

Understanding the Effects of Dielectric Property, Separation Distance, and Band Alignment on Interlayer Excitons in 2D Hybrid MoS₂/WSe₂ Heterostructures

Jaehoon Ji and Jong Hyun Choi*

School of Mechanical Engineering, Purdue University
West Lafayette, Indiana 47907, United States

*Corresponding author: jchoi@purdue.edu

Abstract

Two dimensional (2D) van der Waals heterostructures from transition metal dichalcogenide (TMDC) semiconductors show a new class of spatially separate excitons with extraordinary properties. The interlayer excitons (X_I) have been studied extensively, yet the mechanisms that modulate X_I are still not well understood. Here, we introduce several organic-layer-embedded hybrid heterostructures, MoS₂/organic/WSe₂, to study the binding energy of X_I . We discover that the dielectric screening of the quasi-particle is reduced with organic molecules due to decreased dielectric constant and greater separation distance between the TMDC layers. As a result, a distinct blueshift is observed in interlayer emission. We also find that the band alignment at the heterointerface is critical. When the organic layer provides a staggered energy state, interlayer charge transfer can transition from tunneling to band-assisted transfer, further increasing X_I emission energies due to a stronger dipolar interaction. The formation of X_I may also be significantly suppressed with electron or hole trapping molecules. These findings should be useful in realizing X_I -based optoelectronics.

Keywords: Interlayer exciton, van der Waals heterostructure, transition metal dichalcogenide, dielectric screening, charge transfer, optoelectronics

Two dimensional (2D) heterostructures built by stacking transition metal dichalcogenides (TMDCs) such as MoS₂ and WSe₂ have garnered much attention due to their extraordinary optoelectronic properties. The strong light-matter interaction in the heterostructures gives rise to interlayer excitons (X_I) which are a bound state of spatially separate electrons and holes in opposite 2D layers.¹ The X_I in heterobilayers such as MoS₂/WSe₂ and MoSe₂/WSe₂ have large binding energies (~110 meV).²⁻⁴ The large energy leads to stable photoluminescence (PL) emission with a long lifetime (~100 ns)⁵ and scalable diffusion length (~a few μ m)⁶. These characteristics make TMDC heterostructures suitable for light-emitting diodes,⁷ photodetectors,⁸ and photovoltaics.⁹ In addition, the separation of charges brings about permanent electric dipoles in the out-of-plane direction of the structure.¹⁰ This allows for electrical control of the interlayer excitons, which may not be possible with individual TMDC layers.¹¹ The exceptional properties and controllability could be harnessed to realize emerging applications such as excitonic devices and valleytronics.¹²

The interlayer excitons in TMDC heterostructures are formed by tunneling of the photogenerated charges through the van der Waals gap between the stacked TMDC heterolayers.¹³ Various mechanisms including chemical doping,² external electrical field,¹⁰ and defects¹⁴⁻¹⁵ were investigated to understand the formation and recombination of X_I. For example, the lifetime of X_I in 2D TMDC heterostructures may be increased by an order of magnitude by photo-irradiation and gate voltage.¹¹ The X_I recombination energy can be also highly tuned (*e.g.*, redshift up to ~100 meV) by applying electrical potential due to the Stark effect.¹⁶ The defects in the heterolayers may allow localized interlayer exciton-polariton interactions, resulting in the enhanced interlayer emission.¹⁴ Despite the extensive studies, understanding the mechanisms that govern X_I and the related emission still remains limited. For example, the dielectric property can change the binding energy of X_I by disrupting the Coulombic interaction between the charges (*i.e.*, electron-hole or e-h). Previous studies mostly focused on the dielectric property of the environment (*e.g.*, various substrates),¹⁷⁻¹⁸ while few studies investigated that of the heterolayers.¹⁹⁻²⁰ Modulating the dielectric properties of the heterostructures, for example, by inserting a layer between TMDC layers, may provide critical insights and novel strategies for tailoring the X_I emission signatures. Further, the insertion of an intermediate layer will necessarily change the separation distance between the photoinduced e-h charges, affecting the X_I characteristics. Such an approach could also help study additional mechanisms that can tailor the interlayer charge transfer process and thus regulate the X_I energy states. The new level of understanding would form the foundation for X_I-based applications.

This work elucidates the dielectric property, the separation gap, and the charge transfer mechanisms between the stacked heterolayers by embedding a uniform layer of organic molecules between them. The 2D MoS₂/organic/WSe₂ hybrid heterostructures show distinct characteristics compared with MoS₂/WSe₂, and the overall properties depend strongly on the nature of the organic molecules. We discover that the dielectric constant of the hybrid heterostructures is reduced by the inserted molecules such as 1,3-bis(3,5-dipyrid-3-ylphenyl)benzene or B3PyPB which has a large energy gap between highest occupied molecular orbital (HOMO) and lowest unoccupied molecular orbital (LUMO). The organic layer also increases the distance between e-h charges in X_I. As a result, the organic-layer-embedded structure exhibits a strong blueshift in the X_I emission. Besides the dielectric screening, we find that the band alignment with the organic layer can also change the interlayer emission drastically. Eosin Y (EY) forms an energy state between MoS₂ and WSe₂, thereby promoting a transition from tunneling to band-assisted transport. Consequently, even higher energy emission (*i.e.*, blueshift in X_I PL) is observed. Further, the interlayer emission may also be suppressed completely when electron or hole trapping layers are used including

tetracyanoquinodimethane (TCNQ) and cobalt phthalocyanine (CoPc), respectively. These findings provide critical insights on the interlayer excitons and should be useful in designing optoelectronic devices from 2D TMDC materials.

To investigate the effects of distinct mechanisms on X_1 , we prepared the organic-molecule-embedded hybrid heterostructures with a sequential stacking method (see Materials and Methods for details).^{2, 21} First, monolayer MoS₂ flakes were placed on a silicon (Si/SiO₂) substrate by mechanical exfoliation.²² The MoS₂ samples were subsequently immersed in the solutions containing dye molecules to form organic layers on top of MoS₂ flakes. Atomic force microscopy (AFM) imaging reveals that the organic molecules, B3PyPB, EY, TCNQ, and CoPc, form uniform layers with an almost identical thickness of ~0.9 nm (Figures S1 and S3; also see SI for details). Then, monolayer WSe₂ was transferred onto the MoS₂/organic sample by polydimethylsiloxane (PDMS) stamping.² MoS₂/WSe₂ heterobilayers were also prepared as a control with the same method except for the solution-incubation step.

The irradiation from a HeNe laser at 633 nm generates interlayer excitons as well as excitons in individual MoS₂ and WSe₂ layers as illustrated in Figure 1a. The staggered energy gap between MoS₂ and WSe₂ facilitates the dissociation of the excitons in each flake, and the photoexcited electrons in WSe₂ and holes in MoS₂ can transfer to the opposite layers via tunneling (Figure 1b).²³ The recombination of the spatially separate electron-hole pair leads to the interlayer emission. The organic layer embedded between MoS₂/WSe₂ can affect the formation of the interlayer excitons and the relevant emission. For example, B3PyPB has a large gap between its HOMO and LUMO levels (~4 eV).²⁴ As such, the tunneling will be the sole mechanism for photoinduced charge transfer in MoS₂/B3PyPB/WSe₂ (as illustrated in Figure 1c), in the same way with the control MoS₂/WSe₂. However, the insertion of an intermediate layer will increase the distance between the TMDC layers and lower the effective dielectric constant of the structure.²⁵ As a result, the energy states of X_1 and related emission will be significantly impacted (*vide infra*).

The organic molecules may also alter the band alignment, thereby causing different charge transfer pathways. EY has a LUMO situated between the CBM of MoS₂ and WSe₂.² As a result, the EY layer will favor the band-assisted transport of photoexcited electrons, while the holes will transfer via tunneling (Figure 1d). Other mechanisms may also be explored such as trapping of the electrons from both TMDC layers by implementing molecules with a LUMO level lower than the MoS₂ CBM. TCNQ is such an exemplary molecule with its LUMO at approximately -4.7 eV. Similarly, one can design hole trapping by constructing a layer of molecules such as CoPc whose HOMO (~-4.9 eV) is higher than the VBM of both MoS₂ and WSe₂. It is worth noting that all four molecular layers have a uniform thickness, and thus the effect of the extended distance between MoS₂ and WSe₂ monolayers will be similar.

Figure 2 shows the effects of the enhanced dielectric constant and the expanded separation distance in the B3PyPB-inserted MoS₂/WSe₂ heterostructure. The control MoS₂/WSe₂ sample exhibits two distinct peaks in the PL spectrum (Figure 2a). The spectral deconvolution with three Gaussian functions (see Figure S2) reveals the interlayer emission at ~801 nm as well as MoS₂ and WSe₂ PL at approximately 668 and 750 nm, respectively.^{2, 26} It is notable that the interlayer emission is stronger than the intralayer PL, which may be attributed to the strong coupling of the spatially separate e-h charges in the TMDC layers, as illustrated in Figure 2b.²³ The sharp features at short wavelengths (around 650 nm) correspond to the Raman scattering of the heterostructure.² In Figure 2c, MoS₂/B3PyPB/WSe₂ displays several distinct features as well as similar characteristics. Its intralayer PL peaks are measured at approximately 665 nm

(MoS₂) and 746 nm (WSe₂) which are slightly blueshifted (by about 3 nm) from the control sample. Figure S4 also presents the PL spectra of individual TMDC flakes with and without organic layers, for a comparison. The excitonic emission energy (E_{PL}) is determined by the bandgap of the material (E_G) and the binding energy of the exciton (E_B): $E_{PL} = E_G - E_B$.²⁷ The nearly invariable energies of intralayer PL emissions from the constituent MoS₂ and WSe₂ indicate that the extent of bandgap renormalization (ΔE_G) due to the insertion of the organic layer is comparable to the change in the binding energies of intralayer excitons (ΔE_B) which may not be significant.²⁸⁻³⁰ In contrast, the interlayer emission appears as a shoulder at ~776 nm which is significantly blueshifted from the control by ~25 nm or ~50 meV. The peak intensity of interlayer emission significantly drops, while that of WSe₂ PL increases by order of magnitude. With the unchanged bandgaps of TMDC layers, the blueshift in X_I emission may be attributed to the reduction of the binding energy of interlayer excitons.

To understand the observed phenomena, we used a simple hydrogen-like particle model to define the energy state of X_I.³¹ Here, we take into account both the dielectric constant of the heterostructure and the separation distance between electron and hole in X_I (see the SI for details). The Hamiltonian (H_{ex}) of the quasi-particle may be expressed as:³²⁻³³

$$H_{ex} = -\frac{\hbar}{2m_{ex}} \frac{1}{\rho} \frac{d}{d\rho} \left[\rho \frac{d}{d\rho} \right] - \frac{e^2}{\epsilon_{ex} \sqrt{\rho^2 + l^2}} \quad (1)$$

where ρ is the relative coordinate, e is an electrical charge, and m_{ex} denotes the effective mass of X_I as $m_{ex}^{-1} = m_e^{-1} + m_h^{-1}$, where m_e and m_h are the mass of electron and hole, respectively, and \hbar is Planck constant. l is the separation length between the charges, and ϵ_{ex} indicates the effective dielectric function of the heterolayers. The eigenvalue of H_{ex} , that is, the binding energy E_B of X_I, is closely related to the shift of interlayer emission and varies as a function of l and ϵ_{ex} . To estimate ϵ_{ex} , we use a simple dielectric model (details shown in the SI Section 5) where each layer is considered as the piecewise dielectric as shown in Figure 2e.³⁴⁻³⁶ Here, the organic layer is the additional, intermediate layer between TMDCs in the hybrid structure. The calculated dielectric function of MoS₂/organic/WSe₂ is $\epsilon_{ex} \approx 5.4$, which is smaller than that of the control (~5.7). The dielectric function can yield the Bohr radius of X_I ($a = \epsilon_{ex} \hbar / m_{ex} e^2$).³⁶⁻³⁷ approximately 1.17 nm for the hybrid and 1.23 nm for the control. The X_I binding energy can then be expressed as a function of the separation distance and Bohr radius or the distance ratio ($x = l/a$), as shown in Figure 2f. The AFM height profiles of the samples in Figures S1 and S3 reveal that the organic-layer-inserted hybrid structures have consistently greater heights than control MoS₂/WSe₂ by ~0.9 nm. With knowledge of the distance and Bohr radius in each sample, we estimate X_I binding energies of the hybrid structure (~81 meV) and the control (~116 meV). The results strongly suggest that the blueshift of interlayer emission (~50 meV) in MoS₂/B3PyPB/WSe₂ may arise from the significant reduction of X_I binding energy (~35 meV) and the renormalized bandgap³⁸ due to the expanded distance and the reduced screening.

Next, we explored EY whose LUMO level is between CBM of WSe₂ and MoS₂. Figure 3a shows the PL spectrum of the MoS₂/EY/WSe₂ heterostructure. Three distinct PL signatures are observed. The intensity and peak positions of MoS₂ (~664 nm) and WSe₂ (~746 nm) are nearly identical with those from MoS₂/B3PyPB/WSe₂. The interlayer emission, however, is measured at around 764 nm, which is even further blueshifted from MoS₂/B3PyPB/WSe₂ by ~12 nm (or ~25 meV). The emission intensity is also stronger by a factor of two. This observation suggests that besides the dielectric screening³⁹, other mechanisms may impact in the energy state of X_I in the EY-inserted heterostructure. Unlike B3PyPB, the EY layer may favor the band-assisted transfer of photoexcited electrons from WSe₂ to MoS₂ due to the staggered band alignment (Figure 3b). As a result, a greater amount of electrons will be transferred in the EY-embedded hybrid structure. Further, the energy barrier between MoS₂ VBM and EY HOMO is much

smaller than that between MoS₂ VBM and B3PyPB HOMO, thus promoting more hole transfer. With the enhanced charge transfer, MoS₂/EY/WSe₂ may have a greater population of electrons in MoS₂ and holes in WSe₂. The EY-inserted heterostructure will thus have a stronger dipole-dipole interaction than the B3PyPB-embedded sample. We attribute this strong dipolar interaction to the origin of the additional blueshift observed in the MoS₂/EY/WSe₂ structure.

The interaction energy (U) originating from the dipole-dipole interaction may be expressed as:⁴⁰

$$U = -\frac{e^2}{\epsilon_{ex}\sqrt{\rho^2 + l^2}} + \frac{2e^2}{\epsilon_{ex}\rho}. \quad (3)$$

where the first term on the right represents the attractive interaction inside the X₁ and the second term stands for the repulsive dipolar interaction between X₁. From the mean-field approximation where the excitons follow the Boltzmann distribution,⁴¹ the average interaction energy of the dipoles (E_{dip}) may be evaluated as

$$E_{dip} = n \int U(\rho)g(\rho)d\rho \quad (4)$$

where n is the dipole density. $g(\rho)$ represents the density distribution of the pair correlation: $g(\rho) = \exp[-U(\rho)/k_B T]$, where T is the temperature and k_B is the Boltzmann constant. The difference in the interaction energy (ΔE_{dip}) responsible for the PL blueshift may be written as:⁴⁰

$$\Delta E_{dip} = \frac{4\pi e^2 l}{\epsilon_{ex}} D\left(\frac{\epsilon_{ex} l k_B T}{e^2} = z\right) \Delta n \quad (5)$$

where D is a bias function with respect to a dimensionless parameter z which is a ratio between thermal and electrostatic energies of the charges ($z \sim 0.13$, in our system). For $z < 1$, D is reduced to a form $D = \frac{\Gamma(4/3)}{2} z^{1/3}$, where Γ is a gamma function.⁴⁰ The model suggests that ΔE_{dip} has a linear relationship with Δn , from which we obtain $\Delta n \sim 2.7 \times 10^{12} \text{ cm}^{-2}$. This is the density difference of photogenerated charges between EY- and B3PyPB-embedded heterostructures (filled red circle in Figure 3d). We recently reported an increased population of the charged particles in hybrid structures, where TMDCs form a staggered band alignment with the organic layers.^{11, 42} With the band-assisted transport at the WSe₂/EY interface, EY-functionalized hybrid structures demonstrate significantly higher electrical currents and photoinduced currents than the control samples without an EY layer. In addition, other studies also reported the energy shift of interlayer emission due to the X₁ density difference. For example, electrical gating can change the X₁ population and demonstrate a blueshift of ~ 20 meV in the interlayer emission,¹⁰ which is consistent with our observation in Figure 3. Laser irradiation also shows a similar correlation between X₁ population and emission energy in 2D heterostructures.⁴³ The results strongly support that the interlayer emission can be tailored by not only dielectric screening, but also dipolar interaction due to the change in the X₁ population with the insertion of an organic layer in the TDMC heterolayers.

We also studied the trapping of photoexcited electrons and holes from the heterostructures, including TCNQ and CoPc layers. Figures 4a and 4b show the PL spectra of MoS₂/TCNQ/WSe₂ and MoS₂/CoPc/WSe₂. The two spectra appear nearly identical, displaying emission peaks at ~ 666 and ~ 746 nm corresponding to MoS₂ and WSe₂, respectively. These spectra are also very similar with those from other heterostructures in Figures 2 and 3. The intralayer excitons may recombine at the valleys of each TMDC layer, where the band energies of one layer are not significantly hybridized with the other layers. Therefore, we conclude that the intralayer emissions from the constituent layers are not significantly affected by the organic layers, which is consistent with our previous study.² In contrast, the interlayer emission is not observed from either sample.

Figures 4c and 4d respectively present the energy band diagrams of the TCNQ- and CoPc-inserted heterostructures, illustrating the quenching mechanisms for interlayer emission. The TCNQ LUMO is located lower than both MoS₂ and WSe₂ CBM. In the same manner, its HOMO is placed below MoS₂ and WSe₂ VBM, thus forming a discontinuously staggered gap at the interfaces. Due to the alignment, the photoexcited electrons from MoS₂ and WSe₂ may be trapped in the TCNQ layer. The trapped charges in TCNQ may not be further transferred to other TMDC layers, because there is no energy state in MoS₂ and WSe₂ near the TCNQ LUMO. As a result, the interlayer exciton formation is suppressed. The CoPc-embedded heterostructure has an opposite band alignment, but displays the same PL characteristics. The LUMO and HOMO levels of CoPc are higher than CBM and VBM of both MoS₂ and WSe₂, respectively. The alignment now favors trapping of holes and prohibits additional hole transfer from CoPc to MoS₂ or WSe₂. Therefore, the interlayer excitons may not be formed in MoS₂/CoPc/WSe₂, thus no related emission is observed. The PL spectra of TCNQ- and CoPc-functionalized individual TMDC flakes in Figure S4 support the trapping behavior of the charges. The TMDC emission intensities are drastically reduced compared to those of the control samples without organic layers. This quenching results from the photoinduced charge transfer at the TMDC/organic interface (see SI for details).

Finally, it is worth noting that the embedded organic layers may not support the radiative recombination of interlayer excitons at the organic/TMDC interfaces. We did not observe any interlayer emission from the hybrid interfaces, for example, MoS₂/B3PyPB and WSe₂/EY. Instead, only a strong quenching was monitored as shown in Figure S4. This strongly suggests that the Coulomb interaction between the charges separately residing in TMDC and organic layers may not be as strong as that in TMDC/TMDC interfaces. Furthermore, the interlayer emission requires both energy and momentum conservation. The lack of radiative recombination leads us to conclude that the organic layers may not compensate the momentum mismatch with TMDC layers due to the relatively weak coupling between organic and TMDC layers compared to the strong interaction at the MoS₂/WSe₂ interface.²

In closing, we have studied the effects of dielectric properties, separation gap, and band alignments on X_I by inserting various organic layers in MoS₂/WSe₂ heterostructures. The organic layers decrease the dielectric constant and expands the separation distance between the TMDCs, together reducing the X_I binding energy. This ultimately leads to a strong blueshift of the interlayer emission. Depending on the types of the energy level alignment, interlayer emission can be further blueshifted by the dipolar interaction, or completely quenched due to the trapping of charges. This approach may be further developed to provide additional controllability on interlayer excitons. For example, the inserted layer may be modified to have periodic patterns by using lithographic techniques.⁴⁴⁻⁴⁵ Such platforms may allow for a study of the localized Coulombic interaction in van der Waals heterostructures⁴⁶ and the physics of exciton-polariton condensates¹⁴. Environmentally sensitive molecules could also be used to tailor interlayer exciton properties by external stimuli, including electro-,⁴⁷ chemo-,⁴⁸ and photo-chromic⁴⁹ molecules. Furthermore, the organic-embedded hybrid heterostructures may be used as a testbed to investigate the interlayer exciton dynamics. The study of organic-TMDC hybrid materials has been limited to characterize the PL lifetime of the intralayer excitons,⁵⁰ while the X_I lifetime is not well understood. The X_I lifetime measurement will contribute to our understanding of light-matter interactions. These efforts could lead to a new class of X_I-based devices with externally tunable characteristics.

Materials and Methods

Sample fabrication. Monolayer MoS₂ flakes were mechanically exfoliated from bulk crystals (SPI Supplies) and deposited on a p-doped Si/SiO₂ substrate. The substrate was ultrasonicated in various solvents, including acetone, methanol, and deionized water (DI) for 30 min each. Then, it was dried by blowing air and placed on a hot plate at 110 °C for 2 min.²² To fabricate the organic layers on top of the MoS₂ flakes, the samples were immersed in the solutions containing the dye molecules at room temperature for 8 h: B3PyPB (1 mg/ml in chloroform), EY (1 mg/ml in ethanol), TCNQ (0.6 mg/ml in chloroform), and CoPc (0.4 mg/ml in dimethylformamide). These molecules are purchased from Sigma-Aldrich in a powder form. The organic-layer/MoS₂ samples were subsequently washed with each solvent of the molecules and DI to remove the loosely bound particles. For example, B3PyPB deposited sample was rinsed with the excess amount of chloroform and then cleaned with DI water.

Top WSe₂ layer was stacked on the prepared organic/MoS₂ sample by a polymer-stamping method.² WSe₂ flakes were first mechanically exfoliated on a dimethylpolysiloxane (PDMS, purchased from Krayden) stamp. The stamp was fabricated by mixing the base and curing agent of PDMS with 12:1 ratio and cured at 65 °C for 12 h. The stamp with a monolayer of WSe₂ was placed on a glass substrate which is connected to a micro-positioner (Signatone). Then, the WSe₂ flake was positioned above the MoS₂/organic layer and brought into contact. The elastomer maintained the position for 30 min at 50 °C and lifted slowly by manipulating the positioner. Finally, the samples were annealed under argon gas environment at 280 °C for 2 h for a better contact at the interface of the heterolayers.

Sample characterization. The optical and Raman measurements were performed using a Renishaw confocal microscope under ambient conditions. A 633-nm HeNe laser at ~0.1 mW was used to irradiate samples through a 100× objective lens. The optical signals of the samples were transferred by the same objective and collected by a charge-coupled device (CCD) camera. The layer numbers of TMDC flakes were first inspected by optical microscopy, and confirmed by the height measurement AFM. A Bruker Dimension Icon AFM was used with a SCANASIST-AIR probe under ambient conditions. To avoid any unwanted effects of the moisture, we baked the samples in the same manner described above before the measurement. The pixel window of 256 × 256 was maintained, and the actual size of the window was adjusted depending on the sizes of samples. The raster-scanning was conducted sequentially after each step of stacking to monitor the thickness of each layer in the heterostructure.

Acknowledgements.

This work was funded by the U.S. National Science Foundation.

References

- (1) Binder, J.; Howarth, J.; Withers, F.; Molas, M. R.; Taniguchi, T.; Watanabe, K.; Faugeras, C.; Wismolek, A.; Danovich, M.; Fal'ko, V. I.; Geim, A. K.; Novoselov, K. S.; Potemski, M.; Kozikov, A. Upconverted electroluminescence via Auger scattering of interlayer excitons in van der Waals heterostructures. *Nature Communications* **2019**, *10*, 2335.
- (2) Ji, J.; Delehey, C. M.; Houpt, D. N.; Heighway, M. K.; Lee, T.; Choi, J. H. Selective Chemical Modulation of Interlayer Excitons in Atomically Thin Heterostructures. *Nano Letters* **2020**, *20*, 2500-2506.
- (3) Rivera, P.; Schaibley, J. R.; Jones, A. M.; Ross, J. S.; Wu, S.; Aivazian, G.; Klement, P.; Seyler, K.; Clark, G.; Ghimire, N. J.; Yan, J.; Mandrus, D. G.; Yao, W.; Xu, X. Observation of long-lived interlayer excitons in monolayer MoSe₂-WSe₂ heterostructures. *Nature Communications* **2015**, *6*, 6242.
- (4) Chiu, M.-H.; Li, M.-Y.; Zhang, W.; Hsu, W.-T.; Chang, W.-H.; Terrones, M.; Terrones, H.; Li, L.-J. Spectroscopic Signatures for Interlayer Coupling in MoS₂-WSe₂ van der Waals Stacking. *ACS Nano* **2014**, *8*, 9649-9656.
- (5) Miller, B.; Steinhoff, A.; Pano, B.; Klein, J.; Jahnke, F.; Holleitner, A.; Wurstbauer, U. Long-Lived Direct and Indirect Interlayer Excitons in van der Waals Heterostructures. *Nano Letters* **2017**, *17*, 5229-5237.
- (6) Yuan, L.; Zheng, B.; Kunstmann, J.; Brumme, T.; Kuc, A. B.; Ma, C.; Deng, S.; Blach, D.; Pan, A.; Huang, L. Twist-angle-dependent interlayer exciton diffusion in WS₂-WSe₂ heterobilayers. *Nature Materials* **2020**, *19*, 617-623.
- (7) Cheng, R.; Li, D.; Zhou, H.; Wang, C.; Yin, A.; Jiang, S.; Liu, Y.; Chen, Y.; Huang, Y.; Duan, X. Electroluminescence and Photocurrent Generation from Atomically Sharp WSe₂/MoS₂ Heterojunction p-n Diodes. *Nano Letters* **2014**, *14*, 5590-5597.
- (8) Xu, Z.; Lin, S.; Li, X.; Zhang, S.; Wu, Z.; Xu, W.; Lu, Y.; Xu, S. Monolayer MoS₂/GaAs heterostructure self-driven photodetector with extremely high detectivity. *Nano Energy* **2016**, *23*, 89-96.
- (9) Cho, A.-J.; Song, M.-K.; Kang, D.-W.; Kwon, J.-Y. Two-Dimensional WSe₂/MoS₂ p-n Heterojunction-Based Transparent Photovoltaic Cell and Its Performance Enhancement by Fluoropolymer Passivation. *ACS Applied Materials & Interfaces* **2018**, *10*, 35972-35977.
- (10) Li, W.; Lu, X.; Dubey, S.; Devenica, L.; Srivastava, A. Dipolar interactions between localized interlayer excitons in van der Waals heterostructures. *Nature Materials* **2020**, *19*, 624-629.
- (11) Jauregui, L. A.; Joe, A. Y.; Pistunova, K.; Wild, D. S.; High, A. A.; Zhou, Y.; Scuri, G.; De Greve, K.; Sushko, A.; Yu, C.-H.; Taniguchi, T.; Watanabe, K.; Needleman, D. J.; Lukin, M. D.; Park, H.; Kim, P. Electrical control of interlayer exciton dynamics in atomically thin heterostructures. *Science* **2019**, *366*, 870-875.
- (12) Liu, Y.; Zhang, S.; He, J.; Wang, Z. M.; Liu, Z. Recent Progress in the Fabrication, Properties, and Devices of Heterostructures Based on 2D Materials. *Nano-Micro Letters* **2019**, *11*, 13.
- (13) Ovesen, S.; Brem, S.; Linderälv, C.; Kuisma, M.; Korn, T.; Erhart, P.; Selig, M.; Malic, E. Interlayer exciton dynamics in van der Waals heterostructures. *Communications Physics* **2019**, *2*, 23.
- (14) Förg, M.; Colombier, L.; Patel, R. K.; Lindlau, J.; Mohite, A. D.; Yamaguchi, H.; Glazov, M. M.; Hunger, D.; Högele, A. Cavity-control of interlayer excitons in van der Waals heterostructures. *Nature Communications* **2019**, *10*, 3697.
- (15) Tongay, S.; Suh, J.; Ataca, C.; Fan, W.; Luce, A.; Kang, J. S.; Liu, J.; Ko, C.; Raghunathanan, R.; Zhou, J.; Ogletree, F.; Li, J.; Grossman, J. C.; Wu, J. Defects activated photoluminescence in two-dimensional semiconductors: interplay between bound, charged and free excitons. *Scientific Reports* **2013**, *3*, 2657.

- (16) Wang, Z.; Chiu, Y.-H.; Honz, K.; Mak, K. F.; Shan, J. Electrical Tuning of Interlayer Exciton Gases in WSe₂ Bilayers. *Nano Letters* **2018**, *18*, 137-143.
- (17) Steinleitner, P.; Merkl, P.; Graf, A.; Nagler, P.; Watanabe, K.; Taniguchi, T.; Zipfel, J.; Schüller, C.; Korn, T.; Chernikov, A.; Brem, S.; Selig, M.; Berghäuser, G.; Malic, E.; Huber, R. Dielectric Engineering of Electronic Correlations in a van der Waals Heterostructure. *Nano Letters* **2018**, *18*, 1402-1409.
- (18) Andersen, K.; Latini, S.; Thygesen, K. S. Dielectric Genome of van der Waals Heterostructures. *Nano Letters* **2015**, *15*, 4616-4621.
- (19) Latini, S.; Winther, K. T.; Olsen, T.; Thygesen, K. S. Interlayer Excitons and Band Alignment in MoS₂/hBN/WSe₂ van der Waals Heterostructures. *Nano Letters* **2017**, *17*, 938-945.
- (20) Fang, H.; Battaglia, C.; Carraro, C.; Nemsak, S.; Ozdol, B.; Kang, J. S.; Bechtel, H. A.; Desai, S. B.; Kronast, F.; Unal, A. A.; Conti, G.; Conlon, C.; Palsson, G. K.; Martin, M. C.; Minor, A. M.; Fadley, C. S.; Yablonovitch, E.; Maboudian, R.; Javey, A. Strong interlayer coupling in van der Waals heterostructures built from single-layer chalcogenides. *Proceedings of the National Academy of Sciences* **2014**, *111*, 6198-6202.
- (21) Zhang, H.; Choi, J.; Ramani, A.; Voiry, D.; Natoli, S. N.; Chhowalla, M.; McMillin, D. R.; Choi, J. H. Engineering Chemically Exfoliated Large-Area Two-Dimensional MoS₂ Nanolayers with Porphyrins for Improved Light Harvesting. *ChemPhysChem* **2016**, *17*, 2854-2862.
- (22) Ji, J.; Choi, J. H. Layer-Number-Dependent Electronic and Optoelectronic Properties of 2D WSe₂-Organic Hybrid Heterojunction. *Advanced Materials Interfaces* **2019**, *6*, 1900637.
- (23) Merkl, P.; Mooshammer, F.; Steinleitner, P.; Girnghuber, A.; Lin, K. Q.; Nagler, P.; Holler, J.; Schüller, C.; Lupton, J. M.; Korn, T.; Ovesen, S.; Brem, S.; Malic, E.; Huber, R. Ultrafast transition between exciton phases in van der Waals heterostructures. *Nature Materials* **2019**, *18*, 691-696.
- (24) Komatsu, R.; Sasabe, H.; Inomata, S.; Pu, Y.-J.; Kido, J. High efficiency solution processed OLEDs using a thermally activated delayed fluorescence emitter. *Synthetic Metals* **2015**, *202*, 165-168.
- (25) Yadav, R. A. K.; Dubey, D. K.; Chen, S.-Z.; Swayamprabha, S. S.; Liang, T.-W.; Jou, J.-H. Effect of dielectric character of electron transporting materials on the performance of organic light-emitting diodes. *MRS Advances* **2018**, *3*, 3445-3451.
- (26) Kunstmann, J.; Mooshammer, F.; Nagler, P.; Chaves, A.; Stein, F.; Paradiso, N.; Plechinger, G.; Strunk, C.; Schüller, C.; Seifert, G.; Reichman, D. R.; Korn, T. Momentum-space indirect interlayer excitons in transition-metal dichalcogenide van der Waals heterostructures. *Nature Physics* **2018**, *14*, 801-805.
- (27) Chernikov, A.; Berkelbach, T. C.; Hill, H. M.; Rigosi, A.; Li, Y.; Aslan, O. B.; Reichman, D. R.; Hybertsen, M. S.; Heinz, T. F. Exciton Binding Energy and Nonhydrogenic Rydberg Series in Monolayer WS₂. *Physical Review Letters* **2014**, *113*, 076802.
- (28) Stergiou, A.; Tagmatarchis, N. Molecular Functionalization of Two-Dimensional MoS₂ Nanosheets. *Chemistry – A European Journal* **2018**, *24*, 18246-18257.
- (29) Amani, M.; Lien, D.-H.; Kiriya, D.; Xiao, J.; Azcatl, A.; Noh, J.; Madhvapathy, S. R.; Addou, R.; KC, S.; Dubey, M.; Cho, K.; Wallace, R. M.; Lee, S.-C.; He, J.-H.; Ager, J. W.; Zhang, X.; Yablonovitch, E.; Javey, A. Near-unity photoluminescence quantum yield in MoS₂. *Science* **2015**, *350*, 1065-1068.
- (30) Khan, Y.; Obaidulla, S. M.; Rezwana Habib, M.; Kong, Y.; Xu, M. Anomalous photoluminescence quenching in DIP/MoS₂ van der Waals heterostructure: Strong charge transfer and a modified interface. *Applied Surface Science* **2020**, *530*, 147213.
- (31) Zhu, X.; Littlewood, P. B.; Hybertsen, M. S.; Rice, T. M. Exciton Condensate in Semiconductor Quantum Well Structures. *Physical Review Letters* **1995**, *74*, 1633-1636.

- (32) Leavitt, R. P.; Little, J. W. Simple method for calculating exciton binding energies in quantum-confined semiconductor structures. *Physical Review B* **1990**, *42*, 11774-11783.
- (33) Trolle, M. L.; Pedersen, T. G.; Vénard, V. Model dielectric function for 2D semiconductors including substrate screening. *Scientific Reports* **2017**, *7*, 39844.
- (34) Florian, M.; Hartmann, M.; Steinhoff, A.; Klein, J.; Holleitner, A. W.; Finley, J. J.; Wehling, T. O.; Kaniber, M.; Gies, C. The Dielectric Impact of Layer Distances on Exciton and Trion Binding Energies in van der Waals Heterostructures. *Nano Letters* **2018**, *18*, 2725-2732.
- (35) Chen, T.; Bowler, N. Analysis of a concentric coplanar capacitive sensor for nondestructive evaluation of multi-layered dielectric structures. *IEEE Transactions on Dielectrics and Electrical Insulation* **2010**, *17*, 1307-1318.
- (36) Kamban, H. C.; Pedersen, T. G. Interlayer excitons in van der Waals heterostructures: Binding energy, Stark shift, and field-induced dissociation. *Scientific Reports* **2020**, *10*, 5537.
- (37) Li, J.; Zhong, Y. L.; Zhang, D. Excitons in monolayer transition metal dichalcogenides. *Journal of Physics: Condensed Matter* **2015**, *27*, 315301.
- (38) Park, Y.; Han, S. W.; Chan, C. C. S.; Reid, B. P. L.; Taylor, R. A.; Kim, N.; Jo, Y.; Im, H.; Kim, K. S. Interplay between many body effects and Coulomb screening in the optical bandgap of atomically thin MoS₂. *Nanoscale* **2017**, *9*, 10647-10652.
- (39) Shokr, F. S. Evaluation of the optical properties of photoconductive Eosin/PMMA nanocomposite film for flexible optoelectronic applications. *Optik* **2017**, *149*, 270-276.
- (40) Laikhtman, B.; Rapaport, R. Exciton correlations in coupled quantum wells and their luminescence blue shift. *Physical Review B* **2009**, *80*, 195313.
- (41) High, A. A.; Leonard, J. R.; Hammack, A. T.; Fogler, M. M.; Butov, L. V.; Kavokin, A. V.; Campman, K. L.; Gossard, A. C. Spontaneous coherence in a cold exciton gas. *Nature* **2012**, *483*, 584-588.
- (42) Choi, J.; Zhang, H.; Choi, J. H. Modulating Optoelectronic Properties of Two-Dimensional Transition Metal Dichalcogenide Semiconductors by Photoinduced Charge Transfer. *ACS Nano* **2016**, *10*, 1671-1680.
- (43) Wang, J.; Ardelean, J.; Bai, Y.; Steinhoff, A.; Florian, M.; Jahnke, F.; Xu, X.; Kira, M.; Hone, J.; Zhu, X.-Y. Optical generation of high carrier densities in 2D semiconductor heterobilayers. *Science Advances* **2019**, *5*, eaax0145.
- (44) Kim, T.; Fan, S.; Lee, S.; Joo, M.-K.; Lee, Y. H. High-mobility junction field-effect transistor via graphene/MoS₂ heterointerface. *Scientific Reports* **2020**, *10*, 13101.
- (45) Kim, J.; Kim, M.-G.; Kim, J.; Jo, S.; Kang, J.; Jo, J.-W.; Lee, W.; Hwang, C.; Moon, J.; Yang, L.; Kim, Y.-H.; Noh, Y.-Y.; Yun Jaung, J.; Kim, Y.-H.; Kyu Park, S. Scalable Sub-micron Patterning of Organic Materials Toward High Density Soft Electronics. *Scientific Reports* **2015**, *5*, 14520.
- (46) Rivera, P.; Yu, H.; Seyler, K. L.; Wilson, N. P.; Yao, W.; Xu, X. Interlayer valley excitons in heterobilayers of transition metal dichalcogenides. *Nature Nanotechnology* **2018**, *13*, 1004-1015.
- (47) Zhang, Y.-M.; Wang, X.; Zhang, W.; Li, W.; Fang, X.; Yang, B.; Li, M.; Zhang, S. X.-A. A single-molecule multicolor electrochromic device generated through medium engineering. *Light: Science & Applications* **2015**, *4*, e249-e249.
- (48) Li, P.; Sui, Q.; Guo, M.-Y.; Yang, S.-L.; Bu, R.; Gao, E.-Q. Selective chemochromic and chemically-induced photochromic response of a metal-organic framework. *Chemical Communications* **2020**, *56*, 5929-5932.
- (49) Kishimoto, Y.; Abe, J. A Fast Photochromic Molecule That Colors Only under UV Light. *Journal of the American Chemical Society* **2009**, *131*, 4227-4229.
- (50) Zhu, T.; Yuan, L.; Zhao, Y.; Zhou, M.; Wan, Y.; Mei, J.; Huang, L. Highly mobile charge-transfer excitons in two-dimensional WS₂/tetracene heterostructures. *Science Advances* **2018**, *4*, eaao3104.

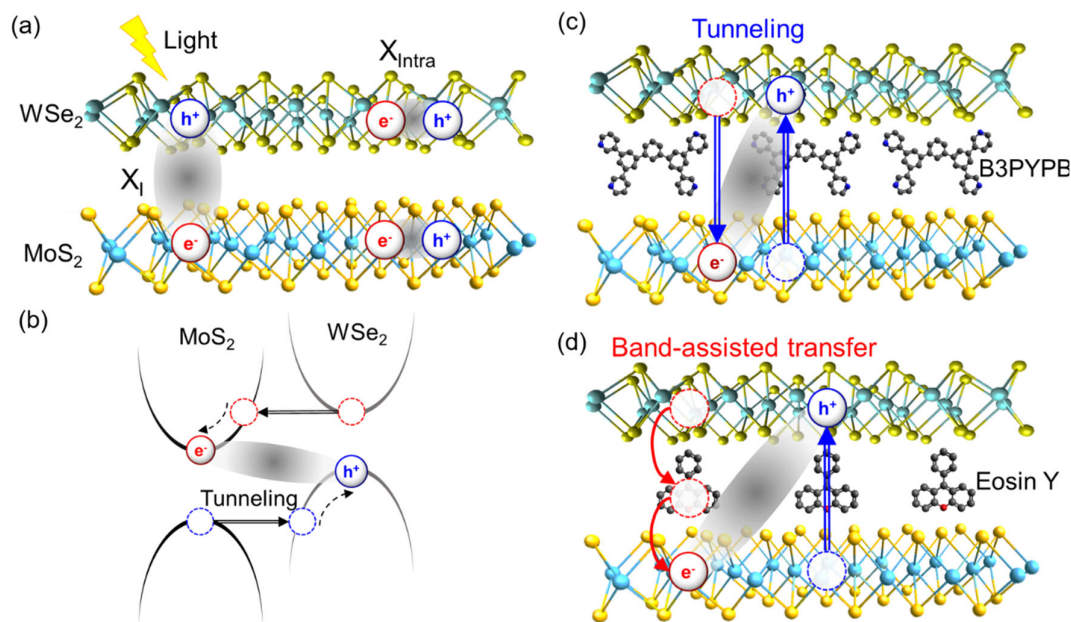


Figure 1. (a) Schematic of a MoS₂/WSe₂ heterostructure. Laser irradiation creates X_I as well as excitons in individual MoS₂ and WSe₂ layers. The Coulomb interaction between the spatially separate electron-hole pair forms a strong bound state as the interlayer exciton. (b) Mechanism for interlayer emission. The photoexcited electron in WSe₂ and hole in MoS₂ transfer to the opposite layers via tunneling facilitated by the staggered band alignment. Schematics of the organic layer embedded hybrid heterostructures: (c) MoS₂/B3PyPB/WSe₂ and (d) MoS₂/EY/WSe₂. The photoinduced charges in the B3PyPB-embedded heterostructure tunnel through the large-energy B3PyPB layer, while the electron transfer via EY is energetically favorable in MoS₂/EY/WSe₂.

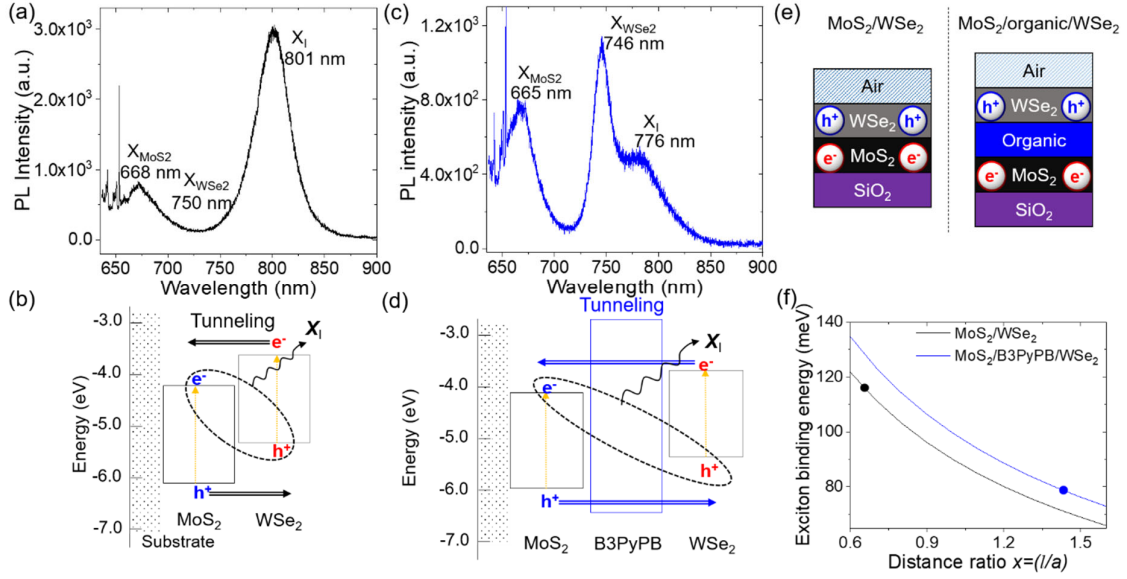


Figure 2. (a) PL spectrum of MoS₂/WSe₂ with a HeNe laser excitation at 633 nm. The deconvolution suggests interlayer emission at ~801 nm as well as PL peaks at ~668 nm (MoS₂) and ~750 nm (WSe₂). (b) Energy diagram of MoS₂/WSe₂ and X_I formation in via tunneling of photoinduced charges. (c) PL spectrum of MoS₂/B3PyPB/WSe₂ showing the interlayer emission with much reduced intensity and a strong blueshift. (d) Energy diagram and schematic of B3PyPB-embedded MoS₂/WSe₂. The organic layer increases the tunneling length and weakens the dielectric screening, resulting in the 25-nm PL shift. (e) Dielectric model of the control MoS₂/WSe₂ (left) and hybrid structure (right). The control sample is modelled with four dielectric layers, while the hybrid structure consists of five dielectric layers, including the organic layer. (f) Theoretical X_I binding energies of MoS₂/B3PyPB/WSe₂ (blue line) and MoS₂/WSe₂ (black line) as a function of distance ratio x . The estimated binding energy difference between the samples (filled black and blue circles, ~50 meV) corresponds to the interlayer emission shift observed with the hybrid heterostructure.

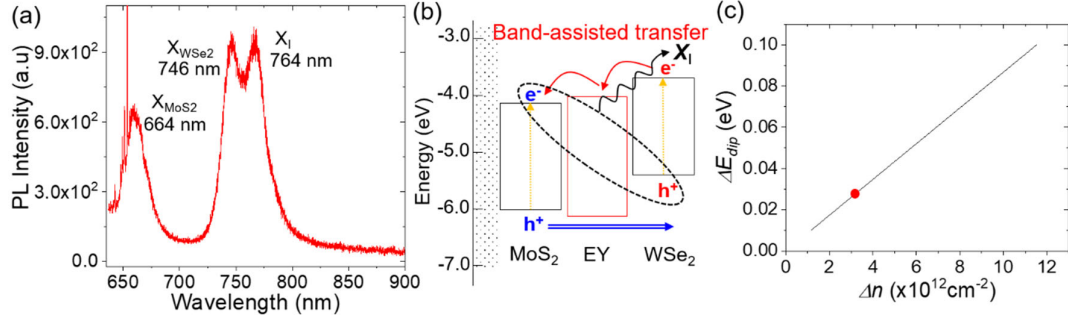


Figure 3. (a) PL spectrum and (b) energy band diagram of MoS₂/EY/WSe₂ heterostructure. Compared to the B3PyPB-inserted sample, the interlayer emission is stronger and blueshifted while intralayer PL signatures are nearly identical. The EY layer facilitates photoinduced electron transfer from WSe₂ to MoS₂ by providing an energy state between their CBM. The energetically favorable band-assisted transfer will thus lead to greater amounts of electrons and holes (*i.e.*, out-of-plane dipoles) than the B3PyPB-embedded heterostructure. (c) A plot of dipolar interaction energy versus the dipole density. The interaction energy linearly increases with the dipole density.

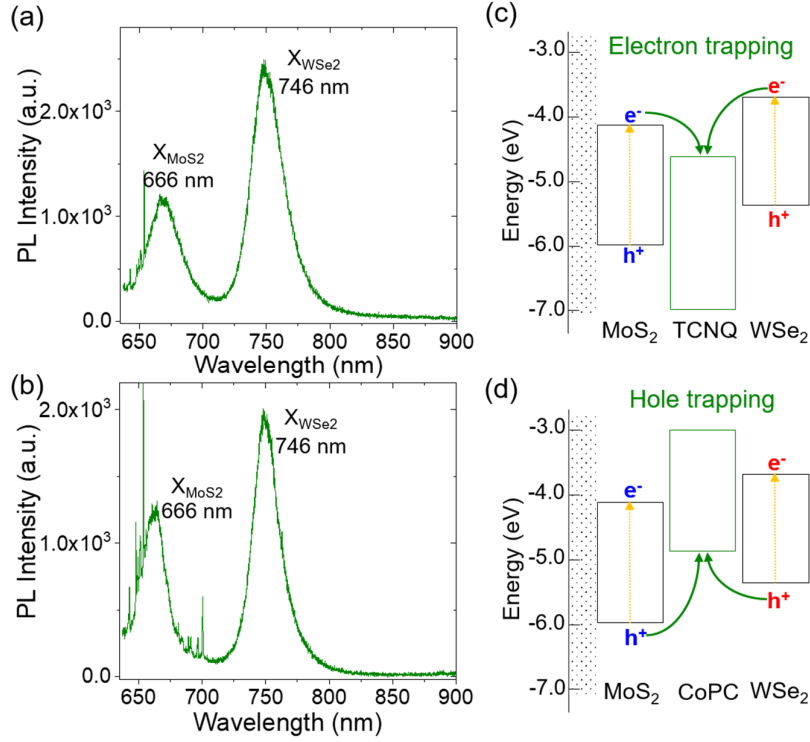


Figure 4. PL spectra of hybrid heterostructures including a layer of (a) TCNQ and (b) CoPc between TMDCs. The intralayer PL spectra are nearly identical, whereas the interlayer emission is not observed from both hybrid heterostructures. Energy band diagrams of (c) MoS₂/TCNQ/WSe₂, favoring electron trapping from both TMDCs, and (d) MoS₂/CoPc/WSe₂, supporting the hole trapping. Both trapping processes induce the complete quenching of X_I emission.

Supporting Information

Understanding the Effects of Dielectric Property, Separation Distance, and Band Alignment on Interlayer Excitons in 2D Hybrid MoS₂/WSe₂ Heterostructures

Jaehoon Ji and Jong Hyun Choi*

School of Mechanical Engineering, Purdue University
West Lafayette, Indiana 47907, United States

*Corresponding author: jchoi@purdue.edu

Content

1. AFM Images and Height Profiles of MoS₂/organic/WSe₂ Hybrid Heterostructures
2. Deconvoluted PL Spectra of MoS₂/organic/WSe₂ Hybrid Heterostructures
3. AFM and PL Measurements of TMDC/organic Samples
4. Solution for 2D Hydrogen-like Schrödinger Problem
5. Dielectric Model
6. References

1. AFM Images and Height Profiles of MoS₂/organic/WSe₂ Hybrid Heterostructures

To characterize each constituent layer in 2D van der Waals structures, direct imaging techniques such as AFM imaging and transmission electron microscopy (TEM) have been adopted in numerous studies.¹⁻⁶ Among the characterization methods, we used AFM imaging to show the layer number of TDMC flakes and the presence of the organic layers in between the TMDC layers. AFM measurement does not damage the crystal structure of the 2D van der Waals heterostructures⁷ and is ideally suited to monitor the hybrid samples. Figure S1 shows the raster-scanned AFM images and the surface profiles of MoS₂/organic/WSe₂ samples and the control MoS₂/WSe₂. All MoS₂/organic/WSe₂ hybrid structures have a uniform thickness around ~2.9 nm, which is consistently higher than that of MoS₂/WSe₂ by ~0.9 nm. This indicates that the organic molecules assemble as a uniform 2D layer between TMDC monolayers.

TEM cross-sectional imaging of the samples may be another option for the characterization. However, one of the inevitable steps in TEM imaging is the slicing of the samples by ion-beam milling or etching the unwanted area.¹⁻² Under the harsh preparation conditions, the hybrid samples may not preserve enough size to distinguish each constituent layer. Moreover, the organic layers in our samples will be vulnerable under the harsh conditions and could be damaged during the preparation.⁸ Therefore, we used AFM and PL measurements (instead of TEM) to confirm the presence of the organic layers. Specifically, we measured additional AFM images of individual flakes with and without the organic layers, and their corresponding PL spectra (see Section 3 below).

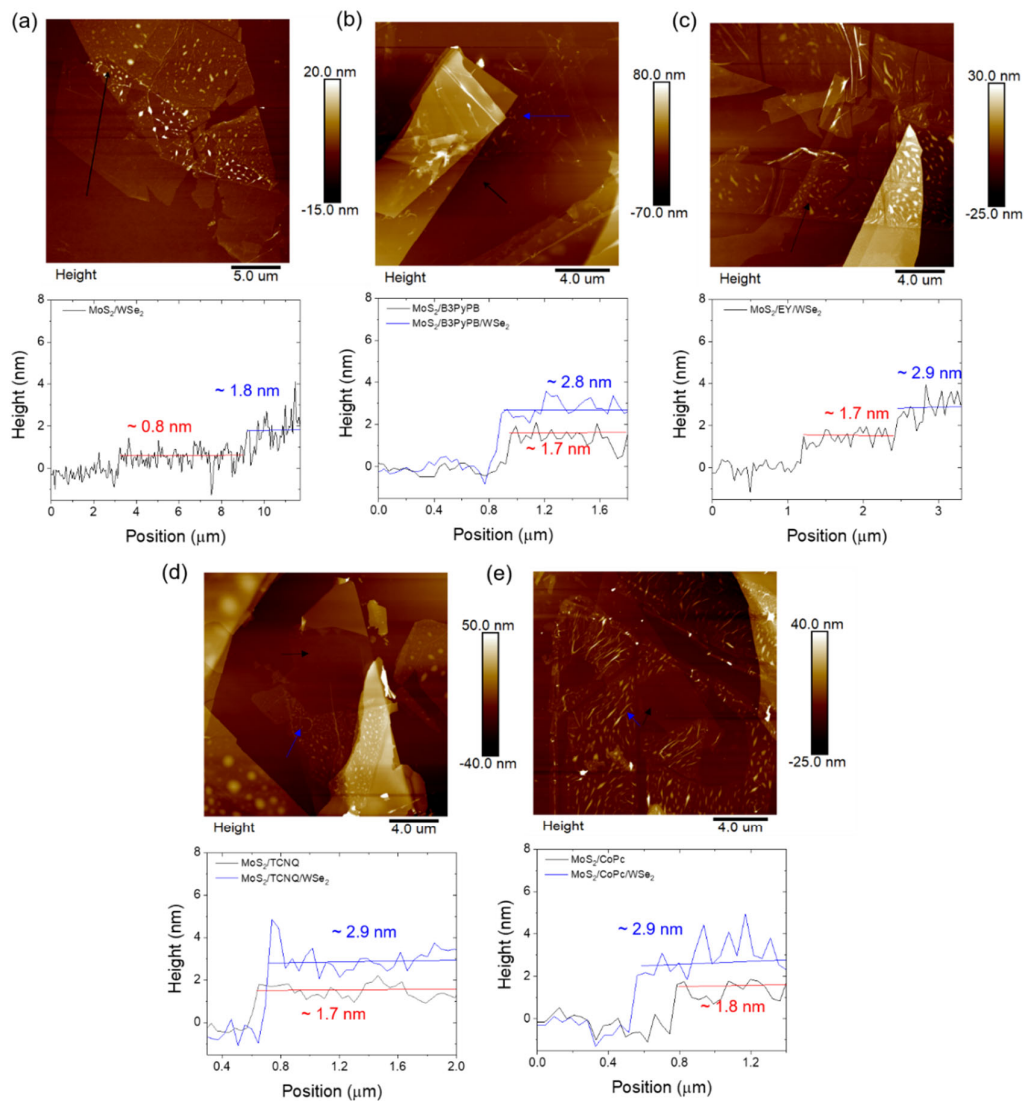


Figure S1. Raster-scanned AFM images and height profiles of (a) $\text{MoS}_2/\text{WSe}_2$ (control), (b) B3PyPB-, (c) EY-, (d) TCNQ-, and (e) CoPc-embedded hybrid-structures, where the organic layers are sandwiched by the TMDC flakes. The height profiles are measured along the arrow lines in the height map.

2. Deconvoluted PL Spectra of MoS₂/organic/WSe₂ Hybrid Heterostructures

The steady-state PL spectra of the samples were measured under the light irradiation with a 633 nm HeNe laser. The temperature-dependent PL spectroscopy may provide insights into the characteristics of interlayer excitons from hybrid heterostructures. However, we did not perform temperature-dependent measurement in this work due to the stability of the organic layers. For example, TCNQ molecules show a phase transition at temperature near 200 K.⁹ The phase transition could deteriorate the quality of the organic layer may deteriorate and induce unwanted effects on the excitons.

To eliminate any temperature-dependent uncertainties, the PL spectra of all the samples were measured at room temperature. Figure S2 shows that intralayer PL emission peaks of MoS₂ and WSe₂ are approximately 666 nm and 746 nm, respectively, for all hybrid heterostructures. The interlayer emission, on the other hand, differs for various organic layers. The control MoS₂/WSe₂ sample exhibits the interlayer emission at ~801 nm; MoS₂/B3PyPB/WSe₂ has X_I peak at ~776 nm; the interlayer emission from MoS₂/EY/WSe₂ is at ~764 nm. No interlayer emission is observed from MoS₂/TCNQ/WSe₂ and MoS₂/CoPc/WSe₂. The detailed mechanisms for the observed phenomena are discussed in the main text.

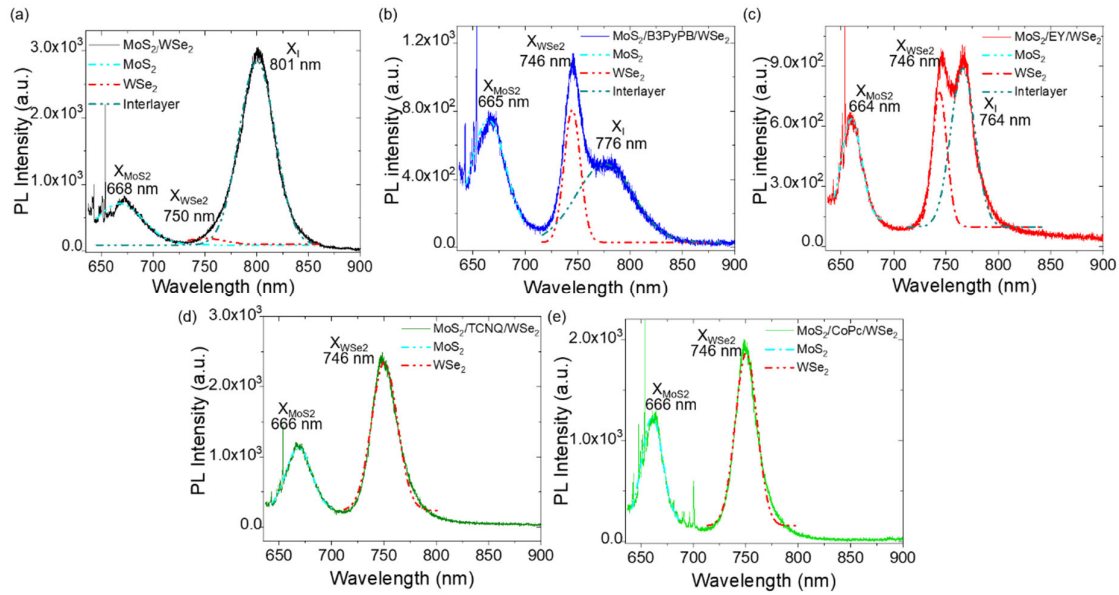


Figure S2. PL spectra of (a) MoS₂/WSe₂ (control), (b) B3PyPB-, (c) EY-, (d) TCNQ-, and (e) CoPc-embedded heterostructures. Three Gaussian profiles are used to deconvolute each PL spectrum: MoS₂ (cyan) and WSe₂ (red), and interlayer emission (dark cyan). The wavelengths of the deconvoluted emission peaks are noted in each figure.

3. AFM and PL Measurements of TMDC/organic Samples

We verified the presence of organic layers on individual TMDC monolayers. The samples were prepared by mechanically exfoliating monolayer TMDC flakes on Si substrates and immersing them in the solutions containing organic molecules (see Materials and Methods for sample preparation details). We measured the thicknesses of MoS₂/B3PyPB and MoS₂/CoPc samples with AFM as shown in Figure S3. The AFM imaging of other TMDC/organic samples (WSe₂/EY and WSe₂/TCNQ) was previously reported elsewhere.⁵⁻⁶ The hybrid structures exhibit a uniform height (~1.7 nm) which is higher than that of the monolayer TMDCs by ~0.9 nm. Note that this height difference is identical with the thickness of the organic layer sandwiched by MoS₂ and WSe₂ in Figure S1.

We also monitor the PL spectra of the individual TMDC monolayers with and without organic layers to investigate the effects of organic layers on individual flakes. Figure S4 shows that the PL intensities of all the TMDC flakes are drastically quenched by the organic layers. We attribute this to the interplay between (i) dark-state doping and (ii) photo-induced charge transfer. (i) As the work function of TMDCs and the reduction potential of organic layers become aligned at the interface, the charge transfer may occur at the interface regardless of the illumination. For example, the reduction potential of B3PyPB (~-2.8 eV) is higher than the work function of MoS₂ (~-4.6 eV).¹⁰ To balance the difference, B3PyPB may donate electrons to MoS₂ (*i.e.*, n-doping), resulting in the reduction of MoS₂ PL (Figure S4a). (ii) Photo-induced charge transfer may also take place at the TMDC/organic interface. For example, WSe₂ CBM is higher than EY LUMO as illustrated in Figure 3b. As a result, photo-induced electrons will migrate from WSe₂ CBM to EY LUMO, thereby quenching the PL of WSe₂ flakes (Figure S4b). Similarly, WSe₂ VBM is located lower than CoPc HOMO (Figure 4d). Due to the built-in potential at the WSe₂/CoPc interface, the holes in the WSe₂ VBM will transition to CoPc MOHO, resulting in a quenching of WSe₂ PL (Figure S4d). More detailed charge transfer mechanisms were discussed in our previous publications.⁵⁻⁶ The AFM images and PL spectra together confirm that uniform 2D organic layers are formed on TMDC flakes, which drastically modulate the PL emission properties of TMDCs.

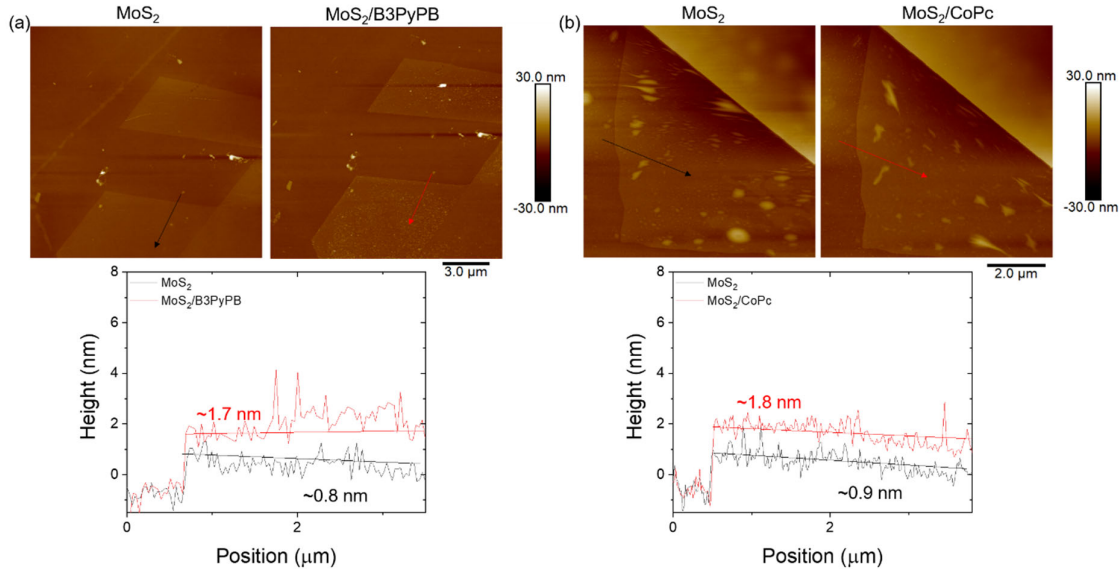


Figure S3 Raster-scanned AFM images and height profiles of (a) MoS₂/B3PyPB and (b) MoS₂/CoPc. The height of individual TMDC monolayers is about 0.8 nm. Compared with the pristine TMDC monolayers, the organic-layer-deposited TMDC flakes have consistently

greater heights by ~ 0.9 nm. This height increase is consistent with the height difference between MoS₂/WSe₂ and MoS₂/organic/WSe₂ (see section 1). The AFM measurements of EY- and TCNQ-deposited TMDC samples were investigated in our previous work.⁶

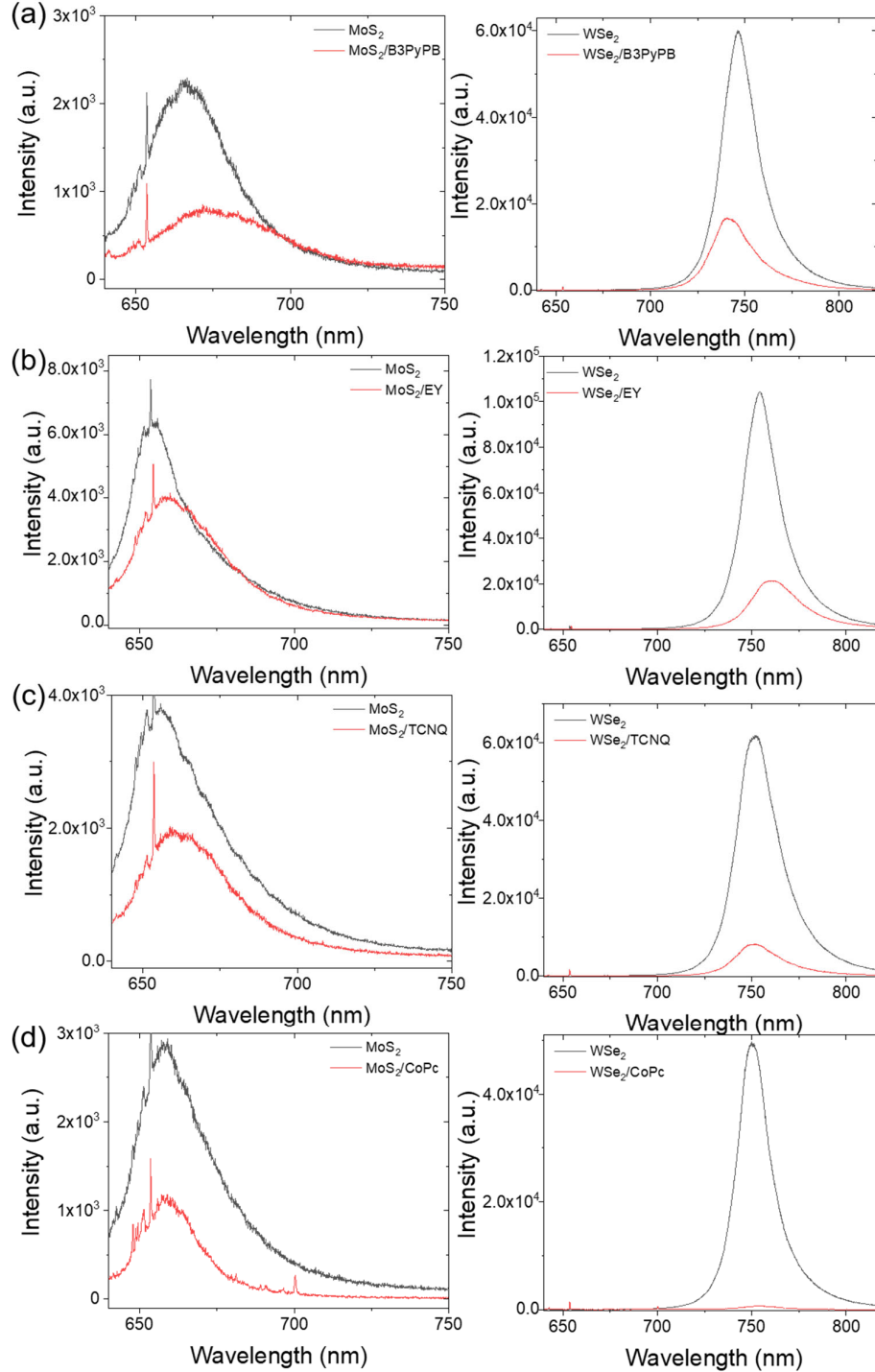


Figure S4. PL spectra of MoS₂ (left) and WSe₂ (right) samples functionalized with (a) B3PyPB, (b) EY, (c) TCNQ, and (d) CoPc layers. All the organic-functionalized TMDC flakes emit significantly weaker PL than the control samples without the organic layers, but the extent of

the modulation depends on the combinations of TMDCs and organic layers. The PL quenching may be attributed to the dark-state doping and the photo-induced charge transfer at the TMDC/organic interface. More detailed discussion on the effects of the organic-functionalization is presented in our previous reports.⁵⁻⁶

4. Solution of 2D Hydrogen-like Schrödinger Problem

An exciton is a quasi-particle formed as a bound state of photoexcited electron and hole, similar to the hydrogen atom with the electrostatic interaction between the constituent charges.¹¹ From the Wannier equation¹², the energy of the particle can be expressed as a sum of the kinetic energy from the relative motion of the charges and the electrostatic interaction within the particle. The eigenvalue of the energy (i.e., exciton binding energy or E_b) can be obtained by solving a Schrödinger equation of the hydrogen-like particle¹³⁻¹⁴:

$$-\frac{\hbar}{2m_{ex}}\frac{1}{\rho}\frac{d}{d\rho}\left[\rho\frac{d\varphi(\rho,l)}{d\rho}\right]-\frac{e^2}{\epsilon_{ex}\sqrt{\rho^2+l^2}}\varphi(\rho,l)=E_b\varphi(\rho,l) \quad (1)$$

where \hbar is the reduced Planck constant ($\hbar = h/2\pi$), e is the electrical charge, ρ is the relative coordinate, m_{ex} denotes the effective mass of the exciton, and l is the separation distance between photoexcited electron and hole residing in MoS₂ and WSe₂, respectively. ϵ_{ex} is the dielectric constant of the exciton.¹⁵⁻¹⁷ φ and E_b are the eigenfunction and eigenvalue, respectively. To simplify the equation, we define the radius of the interlayer exciton as $a = \epsilon_{ex}\hbar/m_{ex}e^2$ and E_{b0} as the binding energy of X₁ without the separation given by l : $E_{b0} = m_{ex}e^4/2\epsilon_{ex}\hbar^2$.¹⁸ The charge separation may be determined by considering the thicknesses of TMDC layers and the intermediate layer.¹⁴ The hybrid structure has the intermediate organic layer with a thickness of ~ 0.9 nm and the separation distance of $l = \sim 1.7$ nm. The l of the control sample without the intermediate layer is set to be ~ 0.8 nm.

From the effective dielectric constant of each structure (see Section 4 below), we obtain $E_{b0} = \sim 114$ meV for the hybrid structure and $E_{b0} = \sim 103$ meV for the control (MoS₂/WSe₂), respectively. The E_{b0} value of the control sample is in excellent agreement with previous reports.¹⁹ From the relationship, the equation (1) may be converted into a dimensionless form:

$$-\frac{1}{y}\frac{d}{dy}\left[y\frac{d\psi}{dy}\right]-\frac{2}{\sqrt{y^2+x^2}}\psi=w(x)\psi \quad (2)$$

where $y = \rho/a$, $x = l/a$, $w(x) = E_b/E_{b0}$, and $\psi = \varphi/a$. The solution of the differential equation can be reduced to the function derived from the curve-fitting method reported by Leavitt *et al.*¹³:

$$w(x) = \frac{4+12.97x+0.718x^2}{1+9.65x+9.24x^2+0.3706x^3} \quad (3)$$

Figure S3 displays the binding energy of the interlayer exciton as a function of the distance ratio x . E_b is inversely proportional to x . As the ratio increases, the exciton binding energy monotonically drops. It implies that with a larger separation gap, the overlap between spatially separate electron and hole becomes weaker, thereby resulting in a smaller binding energy.

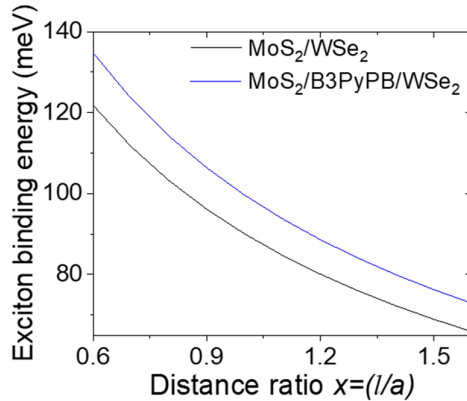


Figure S5. Theoretical prediction of the interlayer exciton binding energies in MoS₂/WSe₂ (black) and B3PyPB-inserted heterostructure (blue) as a function of distance ratio x . The X₁ binding energy decreases monotonically with increasing distance ratio.

5. Dielectric Model

The Coulomb interaction between the charges in X_I highly depends on the dielectric screening of the quasi-particle. To account for the dielectric properties within the heterostructure, a dielectric model is used with a multi-layer Poisson's equation.¹⁵ As illustrated in Figure 2e, five-layers and four-layers of piecewise dielectrics are modelled to reflect the dielectric properties of the organic-inserted structure and the control sample (without an organic layer), respectively. ε_i in Figure 2e represents the relative dielectric constant of the i_{th} layer of the heterostructure. The bottom layer SiO_2 has a dielectric constant of ~ 3.9 , while the top layer, air, has the constant near 1. Both TMDC layers have similar dielectric properties (~ 9.7 for MoS_2 and ~ 10.6 for WSe_2).¹⁴ The intermediate organic layer between TMDCs has a dielectric constant of ~ 3 .^{15, 20-22} For charges in z and z' planes, the electrostatic potential (Φ) with in-plane coordinate ρ can be expressed as:¹⁴

$$-V(\rho, z, z') = \frac{1}{4\pi^2} \int \Phi(z, z', k) e^{ik\rho} d^2k, \quad (4)$$

where the potential V satisfies the Poisson's equation and k is the inverse of the distance of the charges.

$$4\pi\delta(z - z') = [k^2\varepsilon(z, k) - \frac{\partial}{\partial z}\varepsilon(z, k)\frac{\partial}{\partial z}]\Phi(z, z', k). \quad (5)$$

As the charges of X_I are confined in TMDC layers, the potential (Φ_{TMDC}) from X_I s has a relationship:

$$\Phi_{\text{TMDC}}(z, z', k) = \varepsilon_{\text{ex}}\Phi(z, z', k). \quad (6)$$

From the five-layer model reported by Chen et al.²³⁻²⁴, the effective dielectric constant (ε_{ex}) of the hybrid structure is estimated to be ~ 5.4 . The control TMDC heterostructure has $\varepsilon_{\text{ex}} = \sim 5.7$ which is obtained by using a four-layer model presented by Kamban et al.¹⁴

6. References

- (1) Withers, F.; Del Pozo-Zamudio, O.; Mishchenko, A.; Rooney, A. P.; Gholinia, A.; Watanabe, K.; Taniguchi, T.; Haigh, S. J.; Geim, A. K.; Tartakovskii, A. I.; Novoselov, K. S. Light-emitting diodes by band-structure engineering in van der Waals heterostructures. *Nature Materials* **2015**, *14*, 301-306.
- (2) Son, J.; Kwon, J.; Kim, S.; Lv, Y.; Yu, J.; Lee, J.-Y.; Ryu, H.; Watanabe, K.; Taniguchi, T.; Garrido-Menacho, R.; Mason, N.; Ertekin, E.; Huang, P. Y.; Lee, G.-H.; M. van der Zande, A. Atomically precise graphene etch stops for three dimensional integrated systems from two dimensional material heterostructures. *Nature Communications* **2018**, *9*, 3988.
- (3) Rooney, A. P.; Kozikov, A.; Rudenko, A. N.; Prestat, E.; Hamer, M. J.; Withers, F.; Cao, Y.; Novoselov, K. S.; Katsnelson, M. I.; Gorbachev, R.; Haigh, S. J. Observing Imperfection in Atomic Interfaces for van der Waals Heterostructures. *Nano Letters* **2017**, *17*, 5222-5228.
- (4) Cui, X.; Lee, G.-H.; Kim, Y. D.; Arefe, G.; Huang, P. Y.; Lee, C.-H.; Chenet, D. A.; Zhang, X.; Wang, L.; Ye, F.; Pizzocchero, F.; Jessen, B. S.; Watanabe, K.; Taniguchi, T.; Muller, D. A.; Low, T.; Kim, P.; Hone, J. Multi-terminal transport measurements of MoS₂ using a van der Waals heterostructure device platform. *Nature Nanotechnology* **2015**, *10*, 534-540.
- (5) Ji, J.; Choi, J. H. Layer-Number-Dependent Electronic and Optoelectronic Properties of 2D WSe₂-Organic Hybrid Heterojunction. *Advanced Materials Interfaces* **2019**, *6*, 1900637.
- (6) Ji, J.; Delehey, C. M.; Houpt, D. N.; Heighway, M. K.; Lee, T.; Choi, J. H. Selective Chemical Modulation of Interlayer Excitons in Atomically Thin Heterostructures. *Nano Letters* **2020**, *20*, 2500-2506.
- (7) Son, Y.; Wang, Q. H.; Paulson, J. A.; Shih, C.-J.; Rajan, A. G.; Tvrdy, K.; Kim, S.; Alfeeli, B.; Braatz, R. D.; Strano, M. S. Layer Number Dependence of MoS₂ Photoconductivity Using Photocurrent Spectral Atomic Force Microscopic Imaging. *ACS Nano* **2015**, *9*, 2843-2855.
- (8) Ullevig, D. M.; Evans, J. F. Measurement of sputtering yields and ion beam damage to organic thin films with the quartz crystal microbalance. *Analytical Chemistry* **1980**, *52*, 1467-1473.
- (9) Averkiev, B.; Isaac, R.; Jucov, E. V.; Khrustalev, V. N.; Kloc, C.; McNeil, L. E.; Timofeeva, T. V. Evidence of Low-Temperature Phase Transition in Tetracene–Tetracyanoquinodimethane Complex. *Crystal Growth & Design* **2018**, *18*, 4095-4102.
- (10) Xiao, L.; Qi, B.; Xing, X.; Zheng, L.; Kong, S.; Chen, Z.; Qu, B.; Zhang, L.; Ji, Z.; Gong, Q. A weak electron transporting material with high triplet energy and thermal stability via a super twisted structure for high efficient blue electrophosphorescent devices. *Journal of Materials Chemistry* **2011**, *21*, 19058-19062.
- (11) Miller, B.; Steinhoff, A.; Pano, B.; Klein, J.; Jahnke, F.; Holleitner, A.; Wurstbauer, U. Long-Lived Direct and Indirect Interlayer Excitons in van der Waals Heterostructures. *Nano Letters* **2017**, *17*, 5229-5237.
- (12) Ovesen, S.; Brem, S.; Linderälv, C.; Kuisma, M.; Korn, T.; Erhart, P.; Selig, M.; Malic, E. Interlayer exciton dynamics in van der Waals heterostructures. *Communications Physics* **2019**, *2*, 23.
- (13) Leavitt, R. P.; Little, J. W. Simple method for calculating exciton binding energies in quantum-confined semiconductor structures. *Physical Review B* **1990**, *42*, 11774-11783.
- (14) Kamban, H. C.; Pedersen, T. G. Interlayer excitons in van der Waals heterostructures: Binding energy, Stark shift, and field-induced dissociation. *Scientific Reports* **2020**, *10*, 5537.
- (15) Florian, M.; Hartmann, M.; Steinhoff, A.; Klein, J.; Holleitner, A. W.; Finley, J. J.; Wehling, T. O.; Kaniber, M.; Gies, C. The Dielectric Impact of Layer Distances on Exciton and Trion Binding Energies in van der Waals Heterostructures. *Nano Letters* **2018**, *18*, 2725-2732.
- (16) Andersen, K.; Latini, S.; Thygesen, K. S. Dielectric Genome of van der Waals Heterostructures. *Nano Letters* **2015**, *15*, 4616-4621.

- (17) Trolle, M. L.; Pedersen, T. G.; Vénard, V. Model dielectric function for 2D semiconductors including substrate screening. *Scientific Reports* **2017**, *7*, 39844.
- (18) Laikhtman, B.; Rapaport, R. Exciton correlations in coupled quantum wells and their luminescence blue shift. *Physical Review B* **2009**, *80*, 195313.
- (19) Van der Donck, M.; Peeters, F. M. Interlayer excitons in transition metal dichalcogenide heterostructures. *Physical Review B* **2018**, *98*, 115104.
- (20) Laturia, A.; Van de Put, M. L.; Vandenberghe, W. G. Dielectric properties of hexagonal boron nitride and transition metal dichalcogenides: from monolayer to bulk. *npj 2D Materials and Applications* **2018**, *2*, 6.
- (21) Li, Y.; Chernikov, A.; Zhang, X.; Rigosi, A.; Hill, H. M.; van der Zande, A. M.; Chenet, D. A.; Shih, E.-M.; Hone, J.; Heinz, T. F. Measurement of the optical dielectric function of monolayer transition-metal dichalcogenides: MoS₂, MoSe₂, WS₂, and WSe₂. *Physical Review B* **2014**, *90*, 205422.
- (22) Yadav, R. A. K.; Dubey, D. K.; Chen, S.-Z.; Swayamprabha, S. S.; Liang, T.-W.; Jou, J.-H. Effect of dielectric character of electron transporting materials on the performance of organic light-emitting diodes. *MRS Advances* **2018**, *3*, 3445-3451.
- (23) Chen, T.; Bowler, N. Analysis of a concentric coplanar capacitive sensor for nondestructive evaluation of multi-layered dielectric structures. *IEEE Transactions on Dielectrics and Electrical Insulation* **2010**, *17*, 1307-1318.
- (24) Chen, T.; Song, J.; Bowler, J. R.; Bowler, N. Analysis of A Concentric Coplanar Capacitive Sensor Using A Spectral Domain Approach. *AIP Conference Proceedings* **2011**, *1335*, 1647-1654.